JOURNAL OF COMPUTATIONAL PHYSICS 66, 411–444 (1986)

Stellarator Expansion Methods for MHD Equilibrium and Stability Calculations

V. E. LYNCH, B. A. CARRERAS, L. A. CHARLTON, L. GARCIA, T. C. HENDER, H. R. HICKS, AND J. A. HOLMES

Martin Marietta Energy Systems, Inc., Oak Ridge National Laboratory, Oak Ridge, Tennessee 37831

Received October 7, 1985; revised January 24, 1986

DEDICATED TO THE MEMORY OF RAYMOND C. GRIMM

Two methods for performing stellarator expansion, or average method, MHD calculations are described. The first method includes the calculation of vacuum, equilibrium, and stability using the Greene and Johnson stellarator expansion in which the equilibrium is reduced to a two-dimensional problem by averaging over the geometric toroidal angle in real space coordinates. In the second method, the average is performed in a system of vacuum magnetic coordinates. Both methods are implemented to utilize realistic vacuum field information, making them applicable to configuration studies and machine design as well as to basic research. Illustrative examples are presented to detail the sensitivities of the calculations to physical parameters, to show numerical convergence, and to show the comparison of these methods with each other and with other methods. © 1986 Academic Press, Inc.

1. INTRODUCTION

There has been a renewal of interest in the stellarator concept in recent years largely because of its potential to provide a steady-state, zero net current fusion device. This interest was triggered by several stellarator experiments and has been accompanied by a proliferation of theoretical and computational research. In the area of MHD much effort has been spent on the formulation and development of computational techniques to solve the formidable three-dimensional stellarator equilibrium problem [1–4]. Because MHD studies for 2-D systems are simpler and faster than for 3-D systems, the stellarator expansion [5], or average method [6, 7], has also become an important approach to theoretical and computational MHD in stellarators [7–16]. This method is derived from an ordering scheme in which the ratio of the helically varying magnetic field to the average toroidal field is taken to be first order in a small parameter δ. While it is possible to consider various orderings between the dimensionless parameters N, β, ε, and δ, it is assumed here that $1/N \sim \beta \sim \varepsilon \sim \delta^2$ where N is the number of field periods, ε is the inverse aspect ratio, and β the plasma beta. This ordering reduces the three-dimen-

0021-9991/86 $3.00

sional stellarator equilibrium problem to the solution of a two-dimensional Grad–Shafranov-type equation, while stability is incorporated by retaining the leading order terms in the expansion of the MHD equations [8, 12, 13]. Equilibrium and stability calculations using the stellarator expansion are similar computationally to those for tokamaks, in which two-dimensional equilibria are employed. The main difference comes from the existence of a vacuum transform and the average helical curvature effect. With the experience of tokamak equilibrium and stability [17–20] as a guide, the development of computationally efficient stellarator expansion computer codes has been straightforward. Although the mathematical progression from tokamak to stellarator expansion models is straightforward, the spectrum of instabilities for the two configurations is quite different, as illustrated, for example, by the increased importance of the interchange modes in stellarators.

In previous applications, the stellarator expansion has been shown to give equilibria in good agreement with three dimensional calculations for moderate and large aspect-ratio planar-axis systems [13, 15, 21]. Such systems include Heliotron-E, Wendelstein VII-A, CLEO, and ATF. The validity of stellarator expansion stability calculations for such devices is supported by experimental results from Heliotron-E, which exhibit instability at the predicted β [22]. A variation of the average method in which the "toroidal" average is performed in vacuum magnetic coordinates allows the treatment of helical axis systems, as long as toroidal effects are strong, and permits the incorporation of the vacuum field in an exact way. Equilibrium calculations using this method are in excellent agreement with three-dimensional calculations for a variety of cases [15].

We will concentrate in this paper on numerical aspects of two average-method approaches: a fixed boundary equilibrium and stability calculation using the "classical' average method in geometric toroidal angle, and a flux coordinate average method in which the average is carried out in vacuum magnetic coordinates. Detailed comparisons of the equilibrium and stability results of these and other methods [1–4, 11, 12, 16] have been presented in other publications (3, 13, 15, 21]. In this paper the two numerical methods are described, and numerical convergence studies are presented. The vacuum field calculation will be described in Section 2, while in Section 3 the equilibrium calculations will be discussed and compared. The stability calculations will be considered in Section 4, and Section 5 will contain a summary.

2. Calculation of the Vacuum Magnetic Fields

In the stellarator configuration, external conductors generate the largest part of the magnetic field, both in the toroidal and poloidal directions. MHD equilibrium and stability properties can be quite sensitive to changes in these vacuum fields. To assess these properties for a given external coil system, it is necessary to calculate

the fields due to the currents in the coils accurately. In the region of the plasma, these vacuum fields satisfy

$$\nabla \times \mathbf{B}^{\text{vac}} = 0, \tag{1}$$

and

$$\nabla \cdot \mathbf{B}^{\text{vac}} = 0. \tag{2}$$

Given the external coil configuration and currents it is possible to calculate the magnetic field at location $\mathbf{r}$ using the Biot–Savart formula

$$\mathbf{B}^{\text{vac}}(\mathbf{r}) = \int_{\text{coils}} \mathbf{J}_c(\mathbf{r}_c) \times (\mathbf{r} - \mathbf{r}_c)/|\mathbf{r} - \mathbf{r}_c|^3 \, dV_c, \tag{3}$$

where $\mathbf{J}_c(\mathbf{r}_c)$ are the current densities in the coils at location $\mathbf{r}_c$ and the integral is taken over the coil volumes dV_c at $\mathbf{r}_c$. Equations (1) and (2) are equivalent to

$$\mathbf{B}^{\text{vac}} = \nabla \Phi^{\text{vac}}, \tag{4}$$

where the magnetic potential function Φ^{vac} satisfies

$$\nabla^2 \Phi^{\text{vac}} = 0. \tag{5}$$

While the latter representation has the desirable property of expressing the magnetic field in terms of a single scalar function, from a numerical standpoint there are advantages to using the Biot–Savart formulation: Assuming that Laplace's equation is solved for Φ^{vac} on a discrete grid, it becomes necessary to interpolate to obtain Φ^{vac} or $\mathbf{B}^{\text{vac}}$ at arbitrary locations. Also, the magnetic field must be obtained by differentiating Φ^{vac}, with an associated loss of numerical accuracy. On the other hand, the Biot–Savart law yields $\mathbf{B}^{\text{vac}}$ directly at arbitrary locations in the plasma region. Here $\mathbf{B}^{\text{vac}}$ is obtained by integration, rather than differentiation. We use the Biot–Savart law to evaluate the vacuum magnetic field due to external conductors. Thus the three-dimensional vacuum fields are not known merely on a finite difference grid, they are represented continuously. Consequently, the integration performed to obtain the Poincaré plots does not require interpolation.

The external conductors are represented by filaments, which we take to be either circles or closed polygons. The polygons need not be planar. For circular coils the fields are given in terms of complete elliptic integrals (which is a more efficient method than a polygonal representation); while for polygonal current configurations having specified number, order, and location of vertices, the magnetic field is also calculated in closed form [23]. Circular filaments are typically used to represent the coils of the poloidal field coil system (PFCS) and the toroidal field coils (if present), while closed polygons are used to describe helical field coils and other noncircular coils. For good numerical accuracy, up to 200 segments are used in each closed polygon to represent a helical field coil.

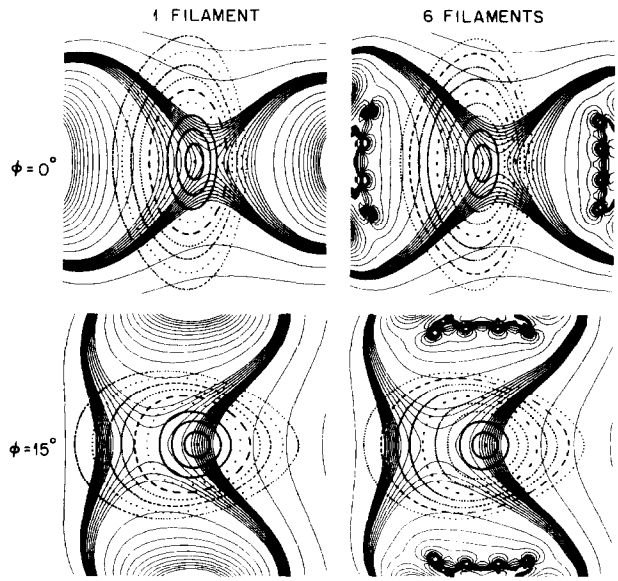

FIG. 1. $|\mathbf{B}^{vac}|$ contours and magnetic field line Poincaré plots of ATF for two toroidal planes separated by one-half field period for helical coils modeled by a single filament and six distributed filaments, respectively.

Distributed coil currents corresponding to the finite cross-sectional areas of each coil, are represented by specifying a number of distinct filaments within the coil cross-section. Such calculations are necessary to accurately determine the magnetic field close to the coils, but are not generally required in equilibrium and stability calculations. This is illustrated in Fig. 1, which shows the $|\mathbf{B}^{vac}|$ contours and magnetic field line Poincaré plots in ATF for two toroidal positions separated by one-half field period. On the left, the helical field coils are each represented by a single filament, while six filaments are used in the figures on the right. It is seen that away from the coils, in the region of Poincaré plots where the plasma is expected to be contained, neither the field lines nor the $|\mathbf{B}^{vac}|$ contours is sensitive to the difference in representation. Only in the vicinity of the coils is the difference noticeable.

The use of the calculated vacuum magnetic field information in the MHD equilibrium and stability average method calculations will be described in Section 3.

3. AVERAGE METHOD EQUILIBRIUM CALCULATIONS

In this section, we describe the average method equilibrium calculations using RSTEQ, a classical stellarator expansion code, and NAV, an average method code in vacuum flux coordinates.

Many of the numerical details of RSTEQ are described elsewhere [18] for a

tokamak version. The present discussion will focus on issues of importance in stellarator calculations. The equations solved [in toroidal (R, ϕ, Z) coordinates] are those of the Greene and Johnson stellarator expansion [5, 13],

$$R\frac{\partial}{\partial R}\frac{1}{R}\frac{\partial \psi}{\partial R}+\frac{\partial^2 \psi}{\partial Z^2}\equiv \Delta^*\psi=-R^2\frac{d\langle P\rangle}{d\psi}-(F+F^*)\frac{dF}{d\psi}+\Delta^*\psi^{\mathrm{vac}}, \tag{6}$$

where ψ is the averaged poloidal flux function, $\langle P\rangle$ is the averaged pressure, $F\equiv R\zeta\cdot\langle \mathbf{B}\rangle$, $\langle \mathbf{B}\rangle$ is the averaged magnetic field, and F^* and ψ^{vac} are defined below. The notation $\langle\ \rangle$ denotes the average taken over a field period of the geometric toroidal angle. Equation (6) is solved numerically using as input the vacuum magnetic field data, $F^*(R, Z)$ and $\psi^{\mathrm{vac}}(R, Z)$, and a $\langle P(\psi)\rangle$ profile. The averaged equilibrium flux is then calculated by requiring either zero toroidal current on each flux surface,

$$\frac{dF}{d\psi}(F+\{F^*\})=-\frac{d\langle P\rangle}{d\psi}\{R^2\}, \tag{7}$$

where $\{\ \}$ denotes average over a $\psi=$ const surface, or by requiring strict flux conservation

$$\iota(\psi)=\iota^{\mathrm{vac}}(\psi). \tag{8}$$

For flux-conserving equilibria, the solution procedure is a straightforward modification of that described in Ref. [18] for the tokamak case. Because of the interest in, and relevance of, zero net current stellarator operation, we consider here the solution of Eqs. (6) and (7), and refer to the previous paper for the solution of the flux-conserving case.

To utilize the calculated vacuum field information in the average method calculations, it is necessary to perform averages over the toroidal angle ϕ (at fixed R, Z) of several quantities that appear as quadratic forms of the vacuum fields. Because it is not possible to average toroidally "through" the physical location of a coil, the domain of this average method is restricted to a region inside the projection of the coils onto a poloidal plane. This constraint provides one of the motivations leading to the development of the average method in magnetic coordinates: to increase the region of solution by following the 3-D excursions of the magnetic field lines in performing "toroidal" averages. This generalized average method will be described below, but we now treat the Greene and Johnson stellarator expansion.

Frequently, vacuum field configurations are dominated by a small number of discrete helical components. For this reason, Fourier decomposition in toroidal angle provides an efficient representation of the vacuum field: in toroidal (R, ϕ, Z) coordinates

$$\mathbf{B}^{\mathrm{vac}}(R, \phi, Z)=\mathbf{B}_0(R, Z)+\sum_{n=1}^{\infty}(\mathbf{B}_n^c(R, Z)\cos n\phi+\mathbf{B}_n^s(R, Z)\sin n\phi). \tag{9}$$

In practice the infinite summation in Eq. (9) can be accurately approximated with only a few harmonics. The projection of these harmonics at specified (R, Z) is given by toroidal integration of the vacuum field over a field period. The quantities required for equilibrium and stability studies are the helical curvature

$$F^*(R, Z) = \frac{-R^2}{F_0} \frac{1}{2} \sum_{n>0} (|\mathbf{B}_n^c|^2 + |\mathbf{B}_n^s|^2), \tag{10}$$

and the averaged vacuum flux function

$$\psi^{\text{vac}}(R, Z) = \psi_0(R, Z) + \psi^*(R, Z), \tag{11}$$

where

$$\psi^*(R, Z) = \frac{-R^3}{F_0} \frac{1}{2} \sum_{n>0} \frac{1}{n} (B_{R,n}^c B_{Z,n}^s - B_{R,n}^s B_{Z,n}^c) \tag{12}$$

is the averaged value of the helical contribution, $F_0 = RB_{\phi 0}$, and ψ_0 is the axisymmetric contribution to the poloidal flux which satisfies

$$\Delta^* \psi_0 = 0, \tag{13}$$

subject to the boundary condition

$$\mathbf{B}_0 = \frac{1}{R} \nabla_\perp \psi_0 \times \hat{\phi}, \tag{14}$$

at the edge of the computational domain.

It is apparent in Eq. (9), and therefore in the subsequent equations, that the computational domain must not intersect the projection of the coils onto the poloidal plane. Within this constraint, however, it is desirable to obtain the averaged vacuum field information over as large a region as possible. The helical quantities $(n \neq 0)$ in Eqs. (10), (12) can be evaluated at any location not intersecting the projection of the coils, but the average vacuum poloidal flux function ψ_0 must be obtained by solving Laplace's equation (13) in some closed region (interior to the coil projection onto a poloidal plane) with the boundary condition given in Eq. (14). More specifically, there are contributions to ψ_0 from the PFCS and from the helical coils. The contribution from circular filamentary PF coils [and toroidal field (TF) coils, if present] can be evaluated at any location not on one of the coils in closed form using elliptic integrals,

$$\psi_{0_{\text{PF}}}(R, Z) = \sum_{\text{PF coils}} \frac{4I_{\text{PF}} R}{ck} \sqrt{R_{\text{PF}}/R} \left\{ \left(1 - \frac{k^2}{2}\right) K(k) - E(k) \right\}, \tag{15}$$

where

$$k^2 = \frac{4R_{\text{PF}} R}{(R_{\text{PF}} + R)^2 + (Z - Z_{\text{PF}})^2}, \tag{16}$$

with I_{PF}, R_{PF}, and Z_{PF} being the current, major radius, and height of the PF coil, respectively. It is the remaining contribution $\psi_{0_{Hel}}$ from the helical coils that must be evaluated using Eq. (13). In this case the boundary condition of Eq. (14) includes only $\mathbf{B}_{0_{Hel}}$, the contribution of the helical coils to the average field $\mathbf{B}_0$. Originally, we employed a rectangular calculation region, but to increase the region size we have subsequently developed a circular region solver, as well. Figure 2 compares the use of these two solvers in application to the ATF coil configuration. The projection of the ATF helical field coils defines a circular region, so that the solver for circular regions provides vacuum information over a greater area than does the square region solver. This is illustrated both by the greater number of flux surfaces enclosed and by the larger range of vacuum flux and rotational transform encompassed (Fig. 2 lower right).

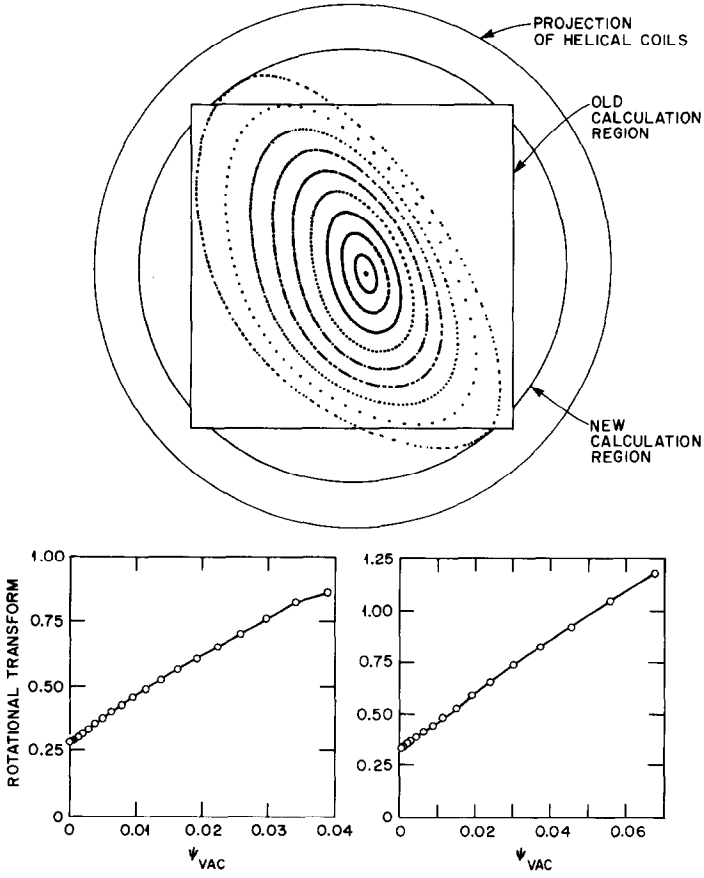

FIG. 2. Magnetic field line Poincaré plot of a toroidal plane of ATF extends outside rectangular calculation region, but is contained in circular region. The edge rotational transform using the rectangular region (left) is less than that of circular region (right).

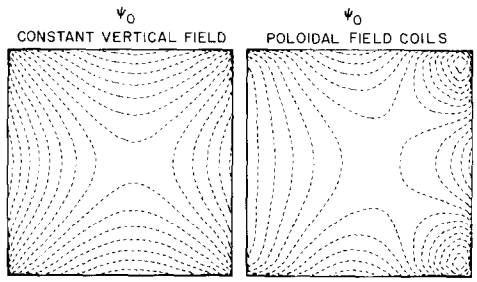

FIG. 3. ψ_0 contours using a constant vertical field (left) and poloidal field coils (right) for ATF.

The sensitivity of ψ_0 to the assumed vertical field is illustrated in Fig. 3 for the ATF coil configuration. The contours resulting from the assumption of a constant vertical field are significantly different from those obtained when a comparable vertical field is generated using actural PF coils, thus stressing the need for careful representation of the vacuum field, particularly for design work. The PF coils supply not only "vertical field" but also other moments that can be used to shape the plasma [14].

In the way the stellarator expansion has been carried out, the properties of the averaged and the pre-averaged fields should agree up to δ^2 terms. This agreement is illustrated in Fig. 4 in which both the rotational transform and the magnetic well are plotted, as functions of the average minor radius, for the original and the averaged vacuum fields of ATF. For ATF $\delta \sim 0.32$, which is consistent with the discrepancies, which are of the order of 10%.

The averaged vacuum information is provided, for use in the calculation of stellarator expansion equilibrium and stability, by specification of the values on a rectangular grid. All quantities are calculated directly at the grid points except for

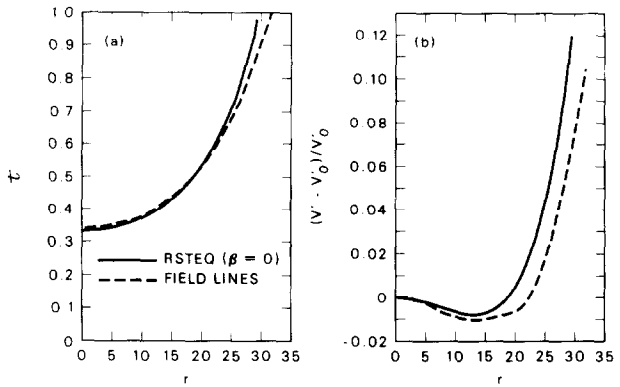

FIG. 4. Rotational transform and magnetic well as functions of average minor radius calculated from ATFs vacuum field lines and its averaged vacuum ψ_0 contours.

$\psi_{0_{\text{Hel}}}$, which is determined by interpolating the solution of Eqs. (13) and (14) obtained as described above. The equilibrium calculations also proceed on a rectangular grid, but the number of grid points and the spatial extent of the grid may be chosen differently from the grid for the averaged vacuum quantities. The mapping of the vacuum quantities onto the equilibrium grid is carried out using bicubic spline interpolation. To represent the vacuum accurately in the subsequent equilibrium and stability calculations, it is necessary to have a sufficiently fine vacuum grid that the bicubic spline fit will be adequate. It has been found that for vacuum grids of 40×40 points or finer (in the R, Z plane), the equilibrium and stability results become independent of the vacuum grid size. Typically, vacuum grid sizes of 100×100 points are used in our stellarator expansion calculations. The vacuum averaging calculations for this classical average method are carried out in the computer code AVAC.

Equation (6) is solved in RSTEQ on a rectangular mesh interior to a chosen (nonrectangular) boundary. This boundary is taken to be a flux surface of the averaged vacuum magnetic field, a surface of constant ψ^{vac}. Normally, the boundary surface is chosen to be as large as possible while remaining a "good" closed surface and containing only such surfaces. In practice, we consider a flux surface to be "good" if in a Poincaré plot the field line appears to describe a surface with toroidal topology. This excludes braided surfaces and stochastic regions. Numerically, the boundary surface is defined by obtaining a cubic spline fit to Z as a function of R through an array of boundary points. These boundary points of constant ψ^{vac} are determined from the two-dimensional vacuum array using bicubic spline interpolation. Normally we assume the averaged configuration be updown symmetric. With this constraint the equilibrium is solved only in the upper half-plane. For most configurations, it is possible to define the boundary as a single-valued function $Z(R)$. For special cases, such as bean shaped plasmas, it is necessary to segment the multiple-valued boundary function into single-valued pieces, but these refinements will not be discussed here. It is also worth noting that there are provisions in RSTEQ for considering analytic models of the vacuum fields (such as a Bessel function model) and also analytic forms for the boundary (such as circular, elliptical, D-shaped, square, bean-shaped, etc.).

Given the boundary specification, Eq. (6) is solved for ψ in the interior subject to the conditions that the boundary is a flux surface of the averaged poloidal flux, $\psi = 0$, and that the averaged pressure goes to zero at at the boundary, $\langle P \rangle = 0$. The latter condition is satisfied whenever the former is, simple by defining the $\langle P(\psi) \rangle$ profile to be zero at $\psi = 0$. To maintain the boundary condition $\psi = 0$, the method of ghost points is used. The ghost points correspond to the points of the rectangular equilibrium coordinate grid that are adjacent to, but outside, the plasma boundary. The boundary value of $\psi = 0$ is maintained by extrapolating the interior values of ψ, using two adjacent interior points in each direction, quadratically to the ghost points with the assumption that ψ passes through zero at the boundary. The solution interior to the boundary is determined iteratively by using the method of successive overrelaxation (SOR) with the ghost points

providing the numerical boundary for this procedure. Because Eq. (6) is nonlinear and must be solved iteratively, it is possible to update the ghost point values periodically during the convergence process.

After solution of Eq. (6), a flux surface analysis of the equilibrium is carried out, again using bicubic splines to determine the points along the constant-ψ surfaces. The surface averaged quantities are obtained using the expression

$$\{f\} = \oint \frac{dl}{|\nabla \Psi|} Rf \Big/ \oint \frac{dl}{|\nabla \Psi|} R, \tag{17}$$

and carrying out the integration over contours of constant ψ using the trapezoidal rule. This information is then used to solve the ordinary differential equation, Eq. (7), for the $F(\psi)$ required to give zero net current within each surface. If a flux conserving equilibrium is desired, a procedure similar to that described in Ref. [18] is followed to determine the $F(\psi)$ required to satisfy Eq. (8). Because this new value of F is not, in general, equal to that which was used to solve the two-dimensional equilibrium, Eq. (6), it is necessary to iterate the solution of Eqs. (6) and (7) until F converges and the zero net current condition is satisfied.

It is appropriate at this point to discuss the advantages and limitations of a fixed boundary approach. The principal advantage is that of control. By specifying the desired shape of the plasma directly, it becomes unnecessary to iterate with coil currents or fluxes on the edges of the computational region to achieve that shape. With this additional degree of control, it is possible to consider the properties of a wide range of cases very quickly. The limitations of the fixed boundary approach are essentially two. First, the plasma boundary for the calculation of a given equilibrium is taken to be one of the vacuum surfaces. However, the presence of small plasma currents slightly distorts this surface. For plasmas characterized by small values of the pressure gradient near the outer boudary, this distorsion is very small, a few percent of the minor plasma radius, at most. The second limitation relates to stability calculations, in that it is not possible to calculate the free boundary stability of low n modes from a fixed boundary equilibrium. Fixed boundary instabilities can be calculated using, for example, a conducting wall boundary condition at the plasma boundary, but there is no vacuum region in the fixed boundary calculation. We address these limitations by also using the free boundary stellarator expansion PEST equilibrium code [11, 12, 17], so that together, the control and convenience of RSTEQ and the free boundary capabilities of PEST provide a comprehensive approach to average method calculations. Extensive comparison of equilibrium and stability calculations [3, 13, 15, 21] using these and other codes [1–4, 11, 12, 16] has provided a coherent picture of the equilibrium and stability of torsatrons, with good agreement between the fixed boundary average method calculations and other methods for a wide range of cases.

It is important, both for the study of equilibrium properties and for stability calculations, to have an accurated numerical representation of the equilibrium, both in terms of the two-dimensional rectangular grid and in the number and spacing of

the flux surface coordinates. For example, the β limit of RSTEQ to achieve numerical convergence increases significantly, more than doubling in some cases, as the grid is made finer. We generally find that, for equal vertical and horizontal grid spacing, equilibrium coordinate grids having 60 or more points horizontally are adequate, giving subsequent equilibrium and stability results that are insensitive to grid spacing. Typically, 100 horizontal points are used in our equilibrium calculations. Similar considerations of the flux coordinate grid show that 60 surfaces provide an adequate representation. Our calculations are generally carried out using 81 flux surfaces, equally spaced in ψ.

Many results obtained using the code RSTEQ have been published [13, 14, 21], including comparisons with those of other equilibrium calculations. We restrict the RSTEQ results presented here to a comparison with those obtained from the generalized average method equilibrium calculations. Before presenting this comparison, we discuss the generalized average method equilibrium as solved in the computer code NAV.

A limitation of the classical average method is that it is not applicable to configurations with magnetic axes having large helical motions. This restriction arises because the method uses a perturbation expansion about a cylindrical state. Koniges and Johnson have developed a method in which the helical swing of the magnetic axis and the minor radius are assumed to be of the same order [24]. An alternate approach for studying helical-axis (and planar-axis) systems is to average toroidally in a system of vacuum flux coordinates [9, 10, 15]. In the flux coordinates, the vacuum fields are axisymmetric and are thus retained to all orders. In contrast, the classical average method retains terms to order δ^2 in the vacuum. An additional benefit of averaging in flux coordinates is that it circumvents the problem in the classical average method associated with the domain over which Laplace's equation (Eq. (13)] is solved. In the flux coordinate average method the domain of solution encompasses the entire region of good flux surfaces. Because the vacuum is retained to all orders, there exists an exact transformation between the vacuum flux coordinates and real space. Thus, after the average equilibrium problem in the vacuum flux coordinates is solved, the solution may be easily projected into real space. In the classical average method, the projection of the equilibrium solution into real space is only accurate to $O(\delta^2)$ and problems occur in mapping outside the region over which the average vacuum problem is solved.

The particular vacuum flux coordinates employed are those described by Boozer [25]. The vacuum magnetic field may be written as

$$\mathbf{B}^{\text{vac}} = \rho_v \nabla \rho_v \times \nabla(\theta_v - \iota \phi_v) \tag{18}$$

or as

$$\mathbf{B}^{\text{vac}} = F_v \nabla \phi_v. \tag{19}$$

Here ρ_v^2 is the poloidal flux and ρ_v acts as a radial coordinate. The magnetostatic

potential ϕ_v is the toroidal coordinate and changes by 2π in one toroidal circuit for an appropriate choice of the constant F_v. The poloidal coordinate θ_v changes by 2π in one poloidal circuit. The $(\rho_v, \theta_v, \phi_v)$ coordinates have the inverse Jacobian

$$D_v = \frac{|\mathbf{B}^{\text{vac}}|^2}{\rho_v F_v}. \tag{20}$$

However, they only have to be calculated once for each vacuum configuration. Therefore the overhead for doing this in the equilibrium calculation is small. The penalty for using such a flux coordinate system is that the metric elements must be calculated. Boozer [25] and Kuo-Petravic *et al.* [26], have described a practical method for calculating the necessary transformations and metric elements for the $(\rho_v, \theta_v, \phi_v)$ coordinate system. From the flux surfaces described by a given coil set, the coordinates are calculated by Fourier analyzing along field lines, which results in Fourier expansions for the cylindrical coordinates R, Z, $\zeta = -\phi$. Thus, for example,

$$R(\rho_v, \theta_v, \phi_v) = \sum_{m,n} R_{m,n}(\rho_v) \cos(m\theta_v + n\phi_v). \tag{21}$$

Only cosine terms need to be retained in this expansion for stellarators that have the property that under the transformations $R \to R$, $Z \to -Z$, $\phi_v \to -\phi_v$, the surfaces are unchanged. For the same reason Z and ζ may be expressed as sine series. Having calculated R, Z, ζ, and D_v in the $(\rho_v, \theta_v, \phi_v)$ coordinates, the necessary metric elements may be calculated. Various inter-relationships show that $g_{\rho\rho}$, $g_{\rho\theta}$, and $g_{\theta\theta}$ are the only independent metric elements. In practice, using the $(\rho_v, \theta_v, \phi_v)$ coordinates directly leads to singularities in some of the dependent variables at $\rho_v = 0$. Such singularities are avoided by rescaling by appropriate powers of ρ_v. The necessary rescalings are $\hat{A}^\theta = \rho_v A^\theta$, $\hat{A}_\theta = A_\theta/\rho_v$, $\hat{g}^{\rho\theta} = \rho_v g^{\rho\theta}$, $\hat{g}_{\rho\theta} = g_{\rho\theta}/\rho_v$, $\hat{g}^{\theta\theta} = \rho_v^2 g^{\theta\theta}$, $\hat{g}_{\theta\theta} = g_{\theta\theta}/\rho_v^2$, and $\hat{D}_v = \rho_v D_v$. These rescalings lead to a system of coordinates that is very similar to ordinary cylindrical coordinates. This method of calculating the coordinate system from a given coil configuration is in accord with our philosophy of trying to match to the vacuum information as accurately as possible.

This generalized average method has been discussed elsewhere [15], so here we focus on those details salient to the numerical method and its implementation. In addition to describing the equations and numerical method, details of convergence tests and comparison of results using the flux coordinate average method with the classical average method and with a 3-D equilibrium calculation will also be given.

The ordering assumptions for the flux coordinate average method are the same as those for the classical average method; namely that the helical fields are of $O(\delta)$ ($\ll 1$) relative to the dominant toroidal fields and that the inverse aspect ratio (ε) satisfies $\varepsilon \sim \delta^2 \sim \beta$. In addition to these orderings, it is also assumed that the equilibrium Shafranov shift is toroidally dominated.

Defining the notation

$$\langle A\rangle_v = \frac{1}{2\pi}\int_0^{2\pi} A\, d\phi_v, \tag{22}$$

where the integral is evaluated at constant ρ_v, θ_v we may write any quantity in terms of its averaged and varying parts in ϕ_v,

$$A = \langle A\rangle_v + \tilde{A}. \tag{23}$$

Then from $\langle \mathbf{V}\cdot\mathbf{B}\rangle_v = 0$ an average flux function χ may be defined by

$$\left\langle \frac{B^\rho}{D_v}\right\rangle_v = \frac{1}{\rho_v}\frac{\partial\chi}{\partial\theta_v} \quad \text{and} \quad \left\langle \frac{B^\theta}{D_v}\right\rangle_v = -\frac{\partial\chi}{\partial\rho_v}. \tag{24}$$

In averaging the product of two terms, there is a quasi-linear contribution to the product:

$$\langle AB\rangle_v = \langle A\rangle_v\langle B\rangle_v + \langle\tilde{A}\tilde{B}\rangle_v. \tag{25}$$

As discussed in Ref. [15], by averaging in the vacuum flux coordinate system, all such quasilinear terms that occur in the averaged equilibrium equations are of high order and need not be retained. In the classical average method, some low order quasilinear terms occur, and they must be explicitly retained. The necessity to retain such quasilinear terms in the classical average method arises because the toroidal averages are taken along paths of constant R, Z that do not follow the vacuum flux surfaces. In contrast, the toroidal averages in the flux coordinate average method [Eq. (22)] are at constant ρ_v, θ_v and do follow the flux surfaces. In summary, therefore, in deriving the equilibrium equations in the vacuum flux coordinates it may be assumed to leading order that the average of a product is the product of the averages.

To leading order, the toroidally averaged radial component of the equilibrium equation ($\mathbf{F} = \mathbf{J}\times\mathbf{B} - \nabla P = 0$) is

$$\left\langle \frac{F_\rho}{D_v}\right\rangle_v = -\left\langle \frac{B^\phi}{D_v}\right\rangle_v \frac{\partial\bar{F}}{\partial\rho_v} + \frac{\partial\chi}{\partial\rho_v}\left[\frac{1}{\rho_v}\frac{\partial}{\partial\rho_v}(\rho_v\langle B_\phi\rangle_v) - \frac{1}{\rho_v}\frac{\partial}{\partial\theta_v}\langle B_\rho\rangle_v\right] - \left\langle\frac{1}{D_v}\right\rangle_v \frac{\partial\langle P\rangle_v}{\partial\rho_v} = 0, \tag{26}$$

where $\bar{F} = \langle B_\phi\rangle_v$ and $\langle B_\rho\rangle_v$, $\langle B_\theta\rangle_v$ may be written in terms of χ and the metric elements in leading order as

$$\langle B_\rho\rangle_v = \frac{\langle D_v g_{\rho\rho}\rangle_v}{\rho_v}\frac{\partial\chi}{\partial\theta_v} - \langle D_v g_{\rho\theta}\rangle_v\frac{\partial\chi}{\partial\rho_v} + \langle D_v g_{\rho\phi}\rangle_v\left\langle\frac{B^\phi}{D_v}\right\rangle_v \tag{27}$$

and

$$\langle B_\theta \rangle_v = \frac{\langle D_v g_{\rho\theta} \rangle_v}{\rho_v} \frac{\partial \chi}{\partial \theta_v} - \langle D_v g_{\theta\theta} \rangle_v \frac{\partial \chi}{\partial \rho_v} + \langle D_v g_{\theta\phi} \rangle_v \left\langle \frac{B^\phi}{D_v} \right\rangle_v . \tag{28}$$

The leading order poloidal and toroidal components of the equilibrium equation are

$$\left\langle \frac{F_\theta}{D_v} \right\rangle_v = -\left\langle \frac{B^\phi}{D_v} \right\rangle_v \frac{1}{\rho_v} \frac{\partial \bar{F}}{\partial \theta} + \frac{1}{\rho_v} \frac{\partial \chi}{\partial \theta} \left[\frac{1}{\rho_v} \frac{\partial}{\partial \rho_v} \rho_v \langle B_\theta \rangle_v - \frac{1}{\rho_v} \frac{\partial}{\partial \theta_v} \langle B_\rho \rangle_v \right]$$
$$- \left\langle \frac{1}{D_v} \right\rangle_v \frac{1}{\rho_v} \frac{\partial \langle P \rangle_v}{\partial \theta_v} = 0 \tag{29}$$

and

$$\rho_v \left\langle \frac{F_\phi}{D_v} \right\rangle = \frac{\partial \chi}{\partial \theta_v} \frac{\partial \bar{F}}{\partial \rho_v} - \frac{\partial \chi}{\partial \rho_v} \frac{\partial \bar{F}}{\partial \theta_v} = 0, \tag{30}$$

respectively. Equation (30) shows that $\bar{F}$ is a function of χ and, similarly, the equilibrium relation $\langle \mathbf{B} \rangle_v \cdot \nabla \langle P \rangle_v = 0$ shows that $\langle P \rangle_v$ is a function of χ only. Equations (26) and (29) may be combined to yield a Grad–Shafranov-type equation

$$\frac{1}{\rho_v} \frac{\partial}{\partial \rho_v} \left(\rho_v \langle g^{\rho\rho} \rangle_v \frac{\partial \chi}{\partial \rho_v} + \langle g^{\rho\theta} \rangle_v \frac{\partial \chi}{\partial \theta_v} \right) + \frac{1}{\rho_v} \frac{\partial}{\partial \theta_v} \left(\langle g^{\rho\theta} \rangle_v \frac{\partial \chi}{\partial \rho_v} + \frac{\langle g^{\theta\theta} \rangle_v}{\rho_v} \frac{\partial \chi}{\partial \theta_v} \right)$$
$$+ \frac{\bar{F}}{F_v} \left[\frac{1}{\rho_v} \frac{\partial}{\partial \rho_v} (\rho_v^2 \iota \langle g^{\rho\rho} \rangle_v) + \frac{1}{\rho^v} \frac{\partial}{\partial \theta_v} (\rho_v \iota \langle g^{\rho\theta} \rangle_v) \right]$$
$$= -\bar{F} \left\langle \frac{1}{D_v} \right\rangle_v \frac{\partial \langle P \rangle_v}{\partial \chi} - \bar{F} \frac{\partial \bar{F}}{\partial \chi}. \tag{31}$$

The equivalence of this equation to that derived in the classical average method [Eq. (6)] may be demonstrated [15]. The Grad–Shafranov equation [Eq. (31)] represents the leading order terms of the toroidally averaged equilibrium equation. In addition, the mathematical elegance of deriving the average equations in the vacuum flux coordinates has also facilitated the derivation of a Poisson-type equation for the leading order toroidally varying components of the equilibrium equation ($\nabla \tilde{P} = \widetilde{\mathbf{J} \times \mathbf{B}}$). These toroidally varying corrections to the equilibrium are of higher order than the average terms, but can be important in some cases, as the grid is made finer. The numerical solution for the toroidally varying corrections has been described in Ref. [15], and these terms will not be considered any further in this paper.

Equation (31) could be solved by a relaxation method similar to that used for the Grad–Shafranov equation derived in the classical average method [Eq. (6)]. A dif-

ferent approach, however, involving an energy minimization technique similar to that used in the Chodura–Schlüter code [2] is used to solve Eq. (31). This method is probably not as efficient computationally but has the advantages of being relatively simple to implement and being flux conserving in the infinite grid limit.

Solving Eq. (31) is of course equivalent to solving the three components of the equilibrium equation [Eqs. (26), (29), and (30)]. To achieve this, an artificial velocity (**v**) is introduced. It is assumed that **v** is a function of ρ_v, θ_v and artificial time (t) only and that $\mathbf{v}\cdot\nabla\phi_v = 0$; the choice of **v** will be described below. Using this velocity, the average pressure is convected,

$$\frac{\partial\langle P\rangle_v}{\partial t} + \mathbf{v}\cdot\nabla\langle P\rangle_v = 0, \tag{32}$$

and the average **B** is advanced in a flux conserving manner (i.e., the ι profile as a function toroidal flux is preserved)

$$\frac{\partial}{\partial t}\left\langle\frac{\mathbf{B}}{D_v}\right\rangle_v = \left\langle\frac{1}{D_v}\nabla\times(\mathbf{v}\times\mathbf{B})\right\rangle_v = \frac{1}{D_v}\nabla\times\left(D_v\mathbf{v}\times\left\langle\frac{\mathbf{B}}{D_v}\right\rangle_v\right). \tag{33}$$

Using Eqs. (32) and (33) we may take the variation of the potential energy in the system. To the same order as the equilibrium expansion we obtain

$$\begin{aligned}\frac{dW}{dt} &= \frac{d}{dt}\int\left(\frac{B^2}{2} - P\right)d^3V \\ &= \int\left(\langle\mathbf{B}\rangle_v\cdot\frac{\partial}{\partial t}\left\langle\frac{\mathbf{B}}{D_v}\right\rangle_v - \left\langle\frac{1}{D_v}\right\rangle_v\frac{\partial\langle P\rangle_v}{\partial t}\right)d\theta_v\,d\rho_v \\ &= -\int\mathbf{v}\cdot\left\langle\frac{\mathbf{F}}{D_v}\right\rangle_v d\theta_v\,d\rho_v,\end{aligned} \tag{34}$$

where the components of $\langle\mathbf{F}/D_v\rangle_v$ are specified in Eqs. (26), (29), and (30). If we choose **v** such that the final integral in Eq. (34) is positive definite then we will minimize the potential energy, and the final state will be $\langle F_\rho/D_v\rangle_v = 0$. The obvious choice is $\mathbf{v} = \langle\mathbf{F}/D_v\rangle_v$; however, as described in Ref. [2] a more efficient scheme is

$$\mathbf{v}^{n+1} = \left\langle\frac{\mathbf{F}}{D_v}\right\rangle_v^{n+1} + v\frac{\overline{|\mathbf{F}/D_v|}^{n+1}}{\overline{|\mathbf{F}/D_v|}^{n}}\mathbf{v}^n. \tag{35}$$

Here, the superscripts denote iteration level, the overhead bar denotes volume average, and for optimal convergence the constant v is chosen just less than unity. This iteration scheme [Eq. (35)] is known as a conjugate gradient scheme. So in summary, Eqs. (32), (33), and (35) constitute an iteration scheme that yields solutions to $\langle F_\rho/D_v\rangle_v = \langle F_\theta/D_v\rangle_v = 0$ [Eqs. (26) and (29)]. To solve the

equilibrium problem [Eq. (31)] we must also satisfy $\langle F_\phi/D_v\rangle_v = 0$ or equivalently have $\bar{F}$ as a function of χ in the final state. From Eqs. (26) and (29) we have,

$$\left\langle \frac{B^\phi}{D_v} \right\rangle_v \left[\frac{\partial \bar{F}}{\partial \theta_v}\frac{\partial \chi}{\partial \rho_v} - \frac{\partial \bar{F}}{\partial \rho_v}\frac{\partial \chi}{\partial \theta_v} \right] + \left\langle \frac{1}{D_v} \right\rangle \left[\frac{\partial \langle P\rangle_v}{\partial \theta_v}\frac{\partial \chi}{\partial \rho_v} - \frac{\partial \langle P\rangle_v}{\partial \rho_v}\frac{\partial \chi}{\partial \theta_v} \right] = 0. \quad (36)$$

The latter bracket is zero because $\langle P\rangle_v$ is a function of χ and therefore, in the final state, $\bar{F}$ is also a function of χ. Thus the solution of Eq. (30) is a consistency requirement on the solutions of Eqs. (30) and (29).

The above iteration scheme is flux conserving. An alternate constraint is that of zero net toroidal current. An additional outer iteration is added to compute such equilibria. This iteration proceeds in the following manner. First, a flux conserving equilibrium is obtained and the net toroidal current (I_T) is computed by flux surface averaging around the contours of constant χ.

The equation

$$I_T = \nabla \phi_v \cdot \nabla \times \langle \mathbf{B}_1 \rangle_v, \quad (37)$$

is then solved by noting that the gauge invariance allows us to specify $\langle B_1^\phi/D_v\rangle_v = 0$. In leading order the expansion, Eq. (37) may then be written as

$$\left\langle \frac{1}{D_v} \right\rangle_v I_T = \frac{1}{\rho_v}\frac{\partial}{\partial \rho_v}\left[\langle D_v g_{\rho\rho}\rangle_v \frac{\partial \chi_1}{\partial \theta_v} - \rho_v \langle D_v g_{\rho\theta}\rangle_v \frac{\partial \chi_1}{\partial \rho_v} \right] - \frac{1}{\rho_v}\frac{\partial}{\partial \theta_v}\left[\langle D_v g_{\rho\theta}\rangle_v \frac{\partial \chi_1}{\partial \theta_v} - \rho_v \langle D_v g_{\theta\theta}\rangle_v \frac{\partial \chi_1}{\partial \rho_v} \right]. \quad (38)$$

The iteration proceeds by solving this equation for [illegible] subtracting [illegible] from [illegible] and [illegible]

Equation (33) may be reduced to an equation for χ,

$$\frac{\partial \chi}{\partial t} + \mathbf{v} \cdot \nabla_\chi = 0 \quad (39)$$

and an equation for the toroidal field

$$\frac{\partial}{\partial t}\left\langle \frac{B^\phi}{D_v} \right\rangle_v = \frac{-1}{\rho_v}\frac{\partial}{\partial \rho_v}\left(\rho_v v^\rho \left\langle \frac{B^\phi}{D_v} \right\rangle_v \right) - \frac{1}{\rho_v}\frac{\partial}{\partial \theta_v}\left(v^\theta \left\langle \frac{B^\phi}{D_v} \right\rangle \right). \quad (40)$$

If $\langle P\rangle_v$ is chosen to be a function of the vacuum χ as an initial condition, then comparing Eqs. (32) and (39) shows that this functional form is preserved for all time. For all the results presented in this paper $\langle P\rangle_v \propto \chi^2$ is used. The equations numerically solved to time advance the average magnetic field are (39) and (40). The radial and poloidal forces [Eqs. (26) and (29)] are then computed with $\langle P\rangle_v$ a given function of χ, and $\mathbf{v}$ is related to these forces by Eq. (35). Centered finite dif-

ferences are used in the radial direction and a Fourier series description is used in the poloidal angle (θ_v). Thus for example

$$\chi(\rho_v, \theta_v, t) = \sum_{m \geq 0} \chi_m(\rho_v, t) \cos m\theta_v. \tag{41}$$

The symmetries inherent in the stellarators studied permit us to retain only cosine terms in Eq. (41). Similarly the other dependent variables $\langle B_\phi / D_v \rangle_v$, $\bar{F}$, and v^ρ are cosine phased and v^θ is sine phased. The temporal differencing is a simple first-order explicit scheme. Such a scheme minimizes the storages in the code but there is a penalty in terms of the admissible time-step sizes. Equation (38), which is solved in the zero net current iteration, is reduced by the θ_v Fourier expansion to a set of coupled second-order ODEs in ρ_v. Taking finite differences in ρ_v then results in a block tridiagonal system which is solved in a standard manner [27].

For the remainder of this section, results will be given for convergence tests of the code NAV, which implements the above algorithms to solve for flux coordinate average method equilibria. In particular, convergence tests will be described for a

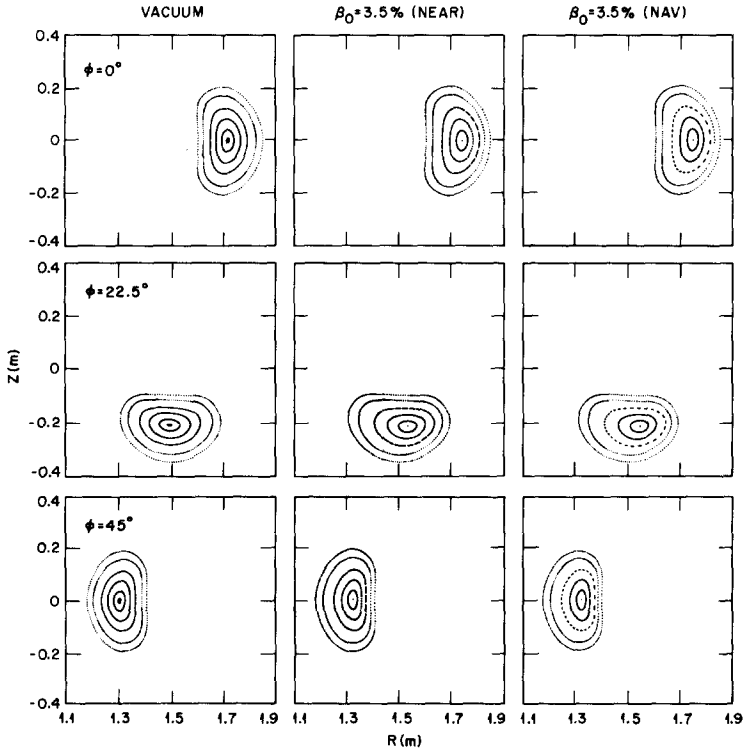

FIG. 5. Equilibrium flux surfaces from NAV, the flux coordinate average method, and NEAR, a fully 3-D method, for a heliac with toroidally dominated equilibrium shift. Three toroidal planes are shown with the vacuum for reference.

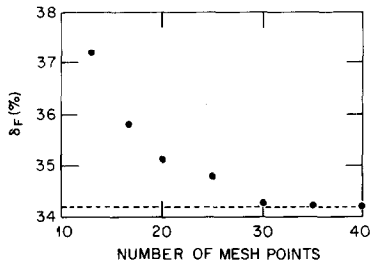

FIG. 6. Equilibrium axis shift of toroidally dominated heliac as a function of number of radial mesh points in NAV for $\beta_0 = 4\%$.

plasma aspect ratio 8, four field period heliac with an ι profile varying between 0.71 at the magnetic axis, and 0.62 at the edge. This case illustrates the ability of the flux coordinate average method to study helical axis equilibria. Figure 5 compares the equilibrium flux surfaces (at $\beta_0 = 3.5\%$) from NAV with a fully 3-D solution from the NEAR code [3]. For this heliac the vacuum flux surfaces are also shown for reference. The relatively low aspect ratio and low ι per field period mean that the equilibrium shift is toroidally dominated for this heliac, and thus the average method is applicable and in good agreement with the 3-D equilibrium solution. The numerical convergence with respect to the radial finite differencing and the poloidal Fourier expansion have been examined. Figure 6 shows how the equilibrium shift (at $\beta_0 = 4\%$) varies with the number of radial mesh points for the heliac shown in Fig. 5. Here, the equilibrium shift (δ_F) is defined as the shift in the vacuum flux coordinate (ρ_v) normalized to the flux coordinate minor radius. The shift is well converged at 30 mesh points. Applying the same convergence test to the poloidal Fourier series representation shows δ_F is converged to within 0.1% when 4 terms are retained in the Fourier series. An alternative measure of the convergence in the poloidal representation comes from examining the magnetic energy spectrum,

$$E_{\chi^m} = \left(\int \chi_m^2 \, dr \right)^{1/2}. \tag{42}$$

Figure 7 compares the E_χ spectrum, for the same case as Fig. 5, with 8 and 4 poloidal modes. This diagnostic of the convergence shows that 4 poloidal modes are sufficient for well converged solutions. In addition to studying the spatial differencing convergence, we must also study the temporal differencing. In all cases studied it has been found that, for the explicit scheme used here, the restriction placed on the timestep by numerical stability is sufficient to ensure temporally converged solutions. Finally, and most importantly, the convergence of the algorithm to a solution of the equilibrium equations must be checked. The volume average of the force ($\overline{|\mathbf{F}/D_v|}$) is a good measure of the convergence of the equilibrium. Typically during an equilibrium calculation the average force is decreased by 7 orders of

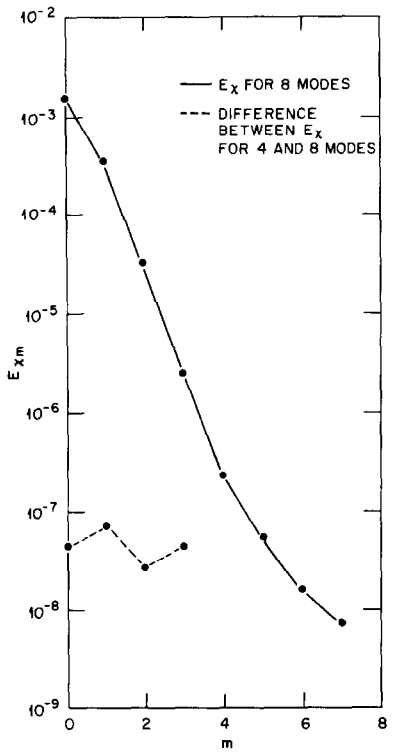

FIG. 7. Difference between E_χ spectrum of toroidally dominated heliac ($\beta_0 = 4\%$) for 4 and 8 poloidal modes.

magnitude. Another sensitive diagnostic of the convergence is the variation of $\bar{F}$ on a constant χ surface

$$[\bar{F}] \equiv \left\{ \left[\int_\chi (\bar{F} - \bar{F}_{AV})^2 \, dl \right] \Big/ \left(\bar{F}_{AV}^2 \int_\chi dl \right) \right\}^{1/2}. \tag{43}$$

Here the integrals are around contours of constant χ, and $\bar{F}_{\mathrm{AV}}$ is the average value of $\bar{F}$ on that surface. Calculations of $[\bar{F}]$ as a function of normalized average radius ($\bar{r}$) for the same case as Fig. 5 with 30 radial mesh points, four modes, and $\beta_0 = 5\%$ shows the equilibrium to be well converged, to within three parts in 10^4.

Next, comparisons will be made between the two equilibrium average method codes described in this paper (RSTEQ, NAV) and a fully 3-D code NEAR [3]. Many such comparisons have been made elsewhere [13, 15, 21], and only a very limited number of examples will be given here for configurations other than ATF. In particular, comparisons will be presented for CLEO [28] which is an $l = 3$, 7-field period stellarator, and for a 24-field period $l = 2$ torsatron. This torsatron is

in fact derived from the 12-field period ATF configuration by doubling the number of field periods and the aspects ratio while holding all other parameters constant.

Figure 8 shows a comparison of the classical and flux coordinate average methods, for a $\beta_0 = 0.4\%$ flux conserving CLEO equilibrium calculation. The close parallel between the two average methods is evident from this figure. It should be

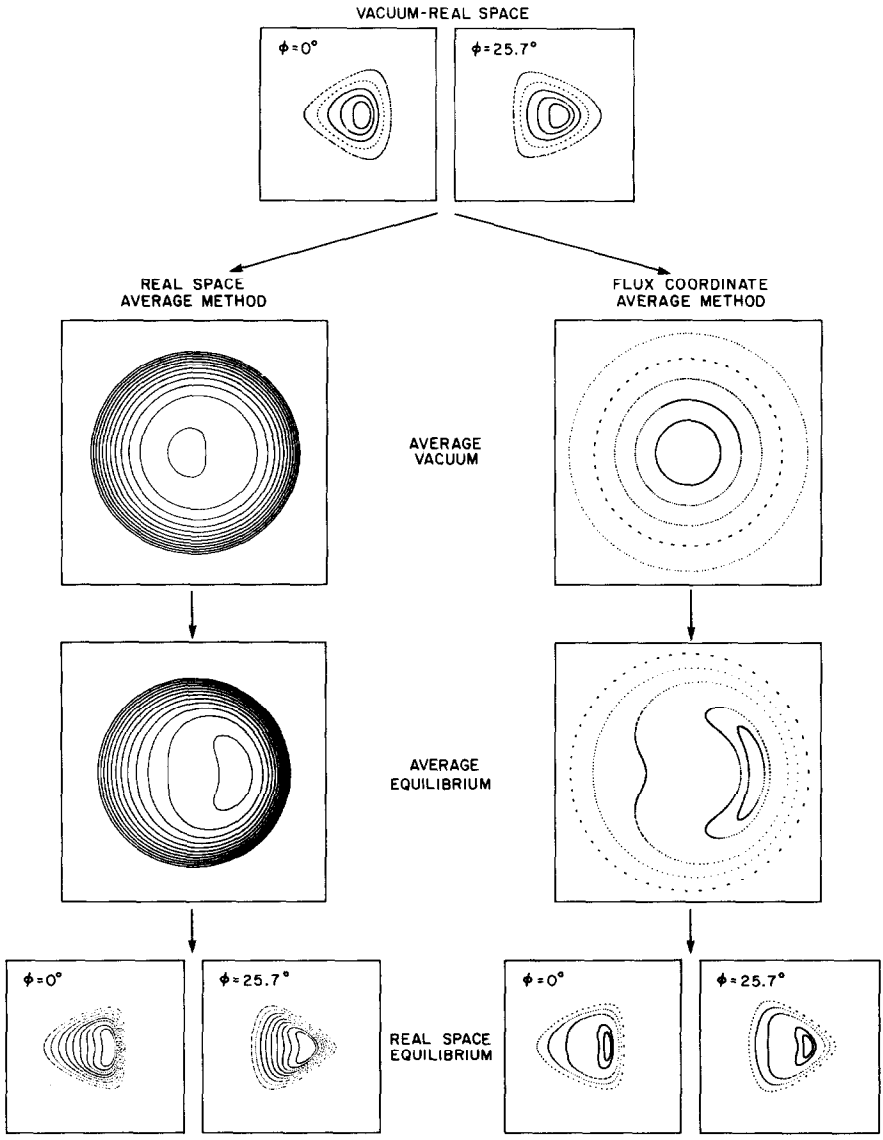

FIG. 8. A comparison of the classical and flux coordinate average methods for a $\beta_0 = 0.4\%$ flux conserving CLEO equilibrium calculation.

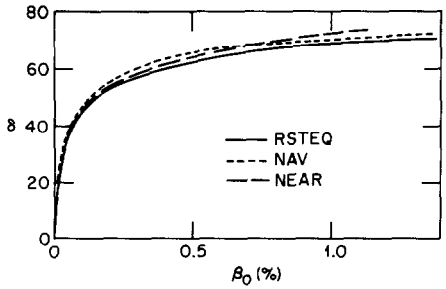

FIG. 9. The equilibrium shift as a function of β_0 for flux conserving CLEO equilibria from the two average method codes (RSTEQ, NAV) and the 3-D NEAR code.

noted that, because of differences in coordinates, the equilibrium solutions can only be compared when they are projected into real space. The equilibrium shifts (δ) for flux conserving CLEO equilibria from the two average method codes (RSTEQ, NAV) are compared with the 3-D NEAR code result, in Fig. 9. Here, δ is defined as the shift in real space normalized to the average minor radius. The magnetic well is a sensitive diagnostic of the surface shape. Figure 10 compares the magnetic well profiles among the three equilibrium codes for flux-conserving CLEO equilibria at $\beta_0 = 0.12\%$. Both Figs. 9 and 10 show very good agreement among the equilibrium codes.

Some comparisons between zero net current equilibria will now be presented for the 24-field period torsatron. Figure 11 shows a comparison of the flux surfaces (at $\beta_0 = 4\%$) computed with the three equilibrium codes for this case. The RSTEQ equilibria appear to have a smaller plasma volume. This arises for the reasons discussed, namely that the equilibrium field lines cannot be followed outside the domain of the average equilibrium solution. Such problems are particularly pronounced in cases where the flux surfaces are very noncircular. For CLEO, where the flux surfaces are more nearly circular, very little plasma volume is lost in projecting the average solution into real space. All such problems are circumvented by

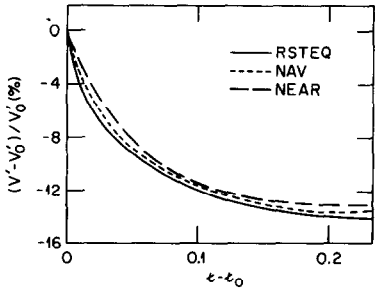

FIG. 10. The magnetic well profiles as a function of ι for flux conserving CLEO equilibria at

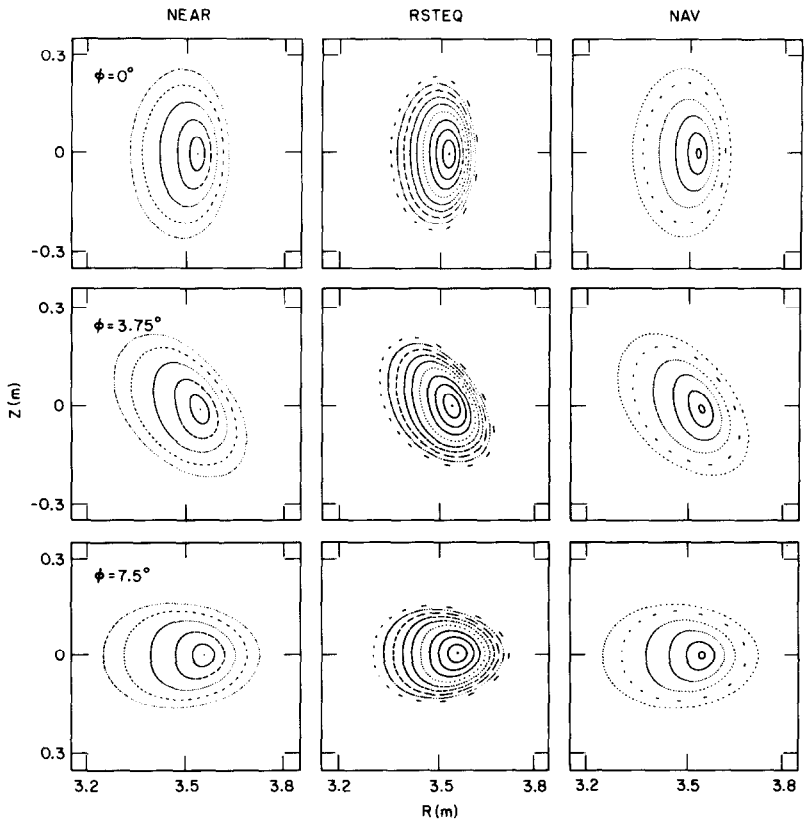

FIG. 11. Zero net current equilibrium flux surfaces for the 24-field period torsatron at $\beta_0 = 4\%$ computed with three codes. Three toroidal planes are shown.

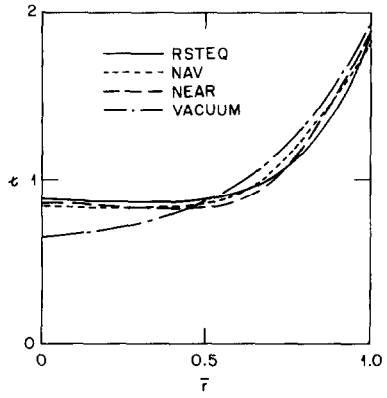

FIG. 12. The ι profiles from the three equilibrium codes for the 24 field period torsatron at $\beta_0 = 6\%$.

the flux coordinate average method where the vacuum information is retained exactly.

The constraint of zero net current causes the ι profile to deform relative to its vacuum shape. Figure 12 shows a comparison of the ι profiles among the three equilibrium codes for the 24 field torsatron at $\beta_0 = 6\%$; also shown for reference is the vacuum ι profile. The V' profiles and the equilibrium shifts as a function of β_0 also show good agreement for this torsatron. In contrast to RSTEQ, both the flux coordinate average method code (NAV) and the 3-D code NEAR have convergence problems for zero net current cases when $\beta_0 \gtrsim 10\%$. The two codes use the same iteration technique to calculate zero net current equilibria and this method fails to converge properly when the pressure-induced currents become large at high β.

4. Stability Calculations

The set of equations used for stability calculations is obtained by applying the stellarator expansion [5] to the full set of MHD equations in toroidal geometry. The basic expansion parameter δ is of the order of the ratio of the helically varying magnetic field to the average toroidal field. The different operators and fields are also expanded in β and $1/N$, where β is the plasma beta and N the number of field periods. Both parameters are taken to be order δ^2. By averaging over the fast variation in the toroidal angle, the resulting equilibrium is two-dimensional, simplifying the stability calculations. The derivation of these equations is similar to the derivation of the reduced set of MHD equations [8] for stellarators but without expansion in the inverse aspect ratio. The assumptions of moderate aspect ratio ($\varepsilon \sim \delta$ or higher) is however needed to close the (fourth order in δ) averaged equations. The set of equations is formally the same as the set derived by Kovrizhnykh and Shchepetov [7], retaining only terms up to order δ^4.

For classical stellarator expansion stability calculations using the MHD equations as embodied in the FAR [20] code it is necessary to map the equilibrium solution into a generalized magnetic coordinate grid. The FAR code uses equilibrium flux coordinates [17, 19, 29]. The various quantities appearing in FAR must be represented as Fourier series in the coordinates Θ (generalized poloidal angle) and ζ (geometric toroidal angle) with coefficients that are functions of ρ (a flux surface coordinate that is thought of as a generalized radius):

$$\psi(\rho, \Theta, \zeta, t) = \sum_{m,n} \psi_{mn}(\rho, t) \cos(m\Theta + n\zeta), \tag{44}$$

where t is the time. Because of up-down symmetry, each quantity may be represented either as a cosine series or a sine series. Because of the axisymmetry of the averaged equilibrium, the equilibrium quantities to be mapped are independent of the toroidal angle ζ as well as the time t,

$$Z(\rho, \Theta) = \sum_{m} Z_m(\rho) \sin m\Theta. \tag{45}$$

Surface quantities, such as ψ_{eq} and $\langle P_{eq} \rangle$, are represented simply as functions of ρ. The mapping is carried out by defining each surface using bicubic spline interpolation, and then using the Jacobian

$$D = 1/R^2, \tag{46}$$

to determine the ρ, θ coordinates according to

$$\rho = \int_{\psi_0}^{\psi} dV/R^2 \Big/ \int_{\psi_0}^{\psi_a} dV/R^2$$

and

$$\theta - \theta_0 = \frac{F}{q} \int_0^l \frac{dl}{R\,|\nabla\psi|}. \tag{47}$$

The expression for ρ involves volume integration interior to the average magnetic surface given by ψ, while that for θ involves integration along the given surface (constant ψ and ρ). With this normalization the coordinates satisfy $0 \leqslant \rho \leqslant 1$ and $0 \leqslant \theta \leqslant 2\pi$. The result of Eq. (47) is a (ρ, θ) poloidal magnetic coordinate grid for the solution of the 2-D stellarator expansion equilibrium. Using bicubic splines it is then possible to evaluate the necessary functions on the (ρ, θ) grid points, which are then projected into the Fourier representation of FAR in a straightforward manner.

The dynamical equations are then solved using a modified version of the initial-value code FAR which incorporates the stellarator expansion terms from the helical averaging. The equilibrium and the equilibrium flux coordinate system used in FAR are calculated using the code RSTEQ described above. The equations are written in terms of potential functions for the magnetic field and fluid velocity, and, in dimensionless form, they are

$$\frac{\partial \psi}{\partial t} = -\frac{\partial \alpha}{\partial \zeta} - v^{\rho} B^{\Theta} + v^{\Theta} B^{\rho} + \eta J_{\zeta} - E_{\zeta}, \tag{48}$$

$$\frac{\partial \chi}{\partial t} = -\frac{1}{\rho}\frac{\partial \alpha}{\partial \Theta} - v^{\zeta} B^{\rho} + v^{\rho} B^{\zeta} + \eta J_{\Theta}, \tag{49}$$

$$\frac{\partial \alpha}{\partial \rho} = -v^{\Theta} B^{\zeta} + v^{\zeta} B^{\Theta} + \eta J_{\rho}, \tag{50}$$

$$\begin{aligned} \frac{\partial U^{\Theta}}{\partial t} = {} & \frac{\partial}{\partial \zeta}(v^{\Theta} U^{\zeta} - v^{\zeta} U^{\Theta}) + \frac{\partial}{\partial \rho}(v^{\Theta} U^{\rho} - v^{\rho} U^{\Theta}) \\ & + S^2 \left[-\frac{\beta_0}{2\varepsilon^2} \left(\frac{\partial R^2}{\partial \zeta}\frac{\partial P}{\partial \rho} - \frac{\partial R^2}{\partial \rho}\frac{\partial P}{\partial \zeta} \right) \right. \\ & \left. + \frac{\partial}{\partial \zeta}(J^{\Theta} B^{\zeta} - J^{\zeta} B^{\Theta}) + \frac{\partial}{\partial \rho}(J^{\Theta} B^{\rho} - J^{\rho} B^{\Theta}) \right], \end{aligned} \tag{51}$$

$$\frac{\partial U^\zeta}{\partial t} = \frac{1}{\rho}\frac{\partial}{\partial \rho}\left[\rho(v^\zeta U^\rho - v^\rho U^\zeta)\right] + \frac{1}{\rho}\frac{\partial}{\partial \Theta}(v^\zeta U^\Theta - v^\Theta U^\zeta)$$
$$+ S^2\left\{-\frac{\beta_0}{2\varepsilon^2}\left[\left(\frac{\partial R^2}{\partial \rho} - \frac{1}{F}\frac{\partial F^*}{\partial \rho}\right)\frac{1}{\rho}\frac{\partial P}{\partial \Theta} - \left(\frac{1}{\rho}\frac{\partial R^2}{\partial \Theta} - \frac{1}{F}\frac{1}{\rho}\frac{\partial F^*}{\partial \Theta}\right)\frac{\partial P}{\partial \rho}\right]\right.$$
$$\left. + \frac{1}{\rho}\frac{\partial}{\partial \rho}\left[\rho(J^\zeta B^\rho - J^\rho B^\zeta)\right] + \frac{1}{\rho}\frac{\partial}{\partial \Theta}(J^\zeta B^\Theta - J^\Theta B^\zeta)\right\}, \tag{52}$$

and

$$\frac{\partial P}{\partial t} = -\left(v^\rho \frac{\partial P}{\partial \rho} + v^\Theta \frac{1}{\rho}\frac{\partial P}{\partial \Theta} + v^\zeta \frac{\partial P}{\partial \zeta}\right). \tag{53}$$

Here, the magnetic field and fluid velocity are given by

$$\mathbf{B} = \nabla\Theta \times \nabla(\rho\chi) + \nabla\zeta \times \nabla\psi \tag{54}$$

and

$$\mathbf{v} = R^2[\nabla\Theta \times \nabla(\rho\Lambda) + \nabla\zeta \times \nabla\Phi] \tag{55}$$

while

$$\mathbf{J} = \nabla \times \mathbf{B}_0, \qquad \mathbf{B}_0 = \mathbf{B} - \nabla\zeta \times \nabla\psi^* \tag{56}$$

and

$$\mathbf{U} = R^2 \nabla \times \mathbf{v}. \tag{57}$$

In Eqs. (48–57), all lengths are normalized to a generalized minor radius a [defined by $a^2 = R_0 \int R^{-2}\, dV/(2\pi^2)$, with the integration over the plasma volume]; the resistivity to η_0 (its value at the magnetic axis); the time to the resistive diffusion time $\tau_r = a^2\mu_0/\eta_0$, where μ_0 is the vacuum magnetic permeability; the magnetic field to B_0 (the toroidal vacuum field at the plasma major radius R_0); the velocity to a/τ_r, and the pressure to P_0 (its equilibrium value at the magnetic axis). R is the major radius coordinate normalized to R_0, and $S = \tau_r/\tau_{Hp}$ is the ratio of the resistive time to the poloidal Alfvén time $[\tau_{Hp} = R_0(\mu_0\rho_m)^{1/2}/B_{\zeta^0}]$.

The new terms appearing in these equations in contrast to the tokamak case are the terms containing ψ^* in the definition of the current, and the modification of the curvature terms in the momentum balance equation due to F^*.

Only linear calculations will be discussed in this paper. A linear eigenfuction with toroidal mode number n is expressed in the FAR code as a superposition of Fourier components,

$$X_n = \sum_m X_{mn}(\rho)\cos(m\Theta + n\zeta) \tag{58}$$

for ψ, χ, and P, and $X_n = \sum_m X_{mn}(\rho)\sin(m\Theta + n\zeta)$ for Λ, Φ, and α. For a given

value of n, however, there are generally multiple unstable eigenfunctions that correspond to different radial mode numbers.

Unless we state otherwise, the calculations shown in this paper are ideal, and only low toroidal mode number ($n \ll N$, where N is the number of field periods of the device) are studied, consistent with the average method assumptions. All the equilibria used in the calculations are zero net current.

Convergence studies with respect to the number of grid points and the number of poloidal modes coupled by toroidicity are needed to get reliable growth rates and eigenfunction spectra. These studies are particularly important for calculating the plasma stability near the marginal stability points.

The configurations used for convergence studies in this paper have helical coil pitch $p_c = 1.4$, where $p_c = N/(lA_c)$, and where $A_c = R_c/a_c$ gives the coil aspect ratio and $l = 2$. This sequence of configurations, which was described in Ref. [13], corresponds to the same pitch as ATF, varying the number of field periods and aspects ratio accordingly.

The configuration $N = 14$ is considered because it illustrates the situation close to the marginal point, where the eigenfunction is strongly localized around the singular surface. This provides a sensitive case for demonstrating numerical convergence, because of the spatial localization. Figure 13 shows the results of a double convergence study for the $n = 2$ eigenfunction. The growth rates are plotted as

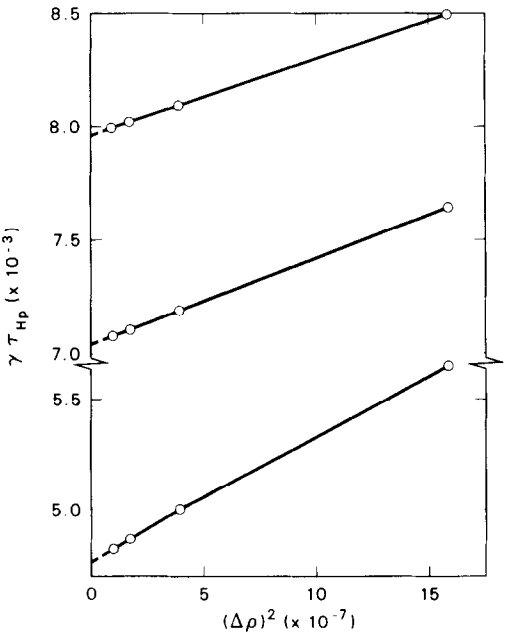

FIG. 13. Linear growth rates of the $n = 2$ mode as a function of the stability grid size for three different equilibria of the $N = 14$ configuration with $\beta_0 = 5.7\%$, each one corresponding to a different equilibrium mesh.

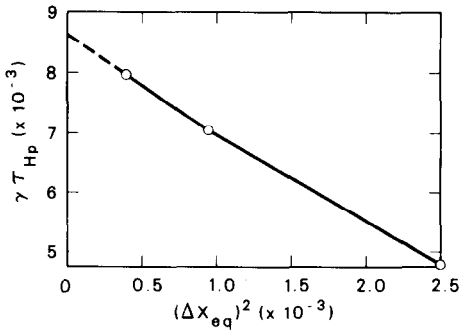

Fig. 14. Converged $n=2$ growth rates as a function of the equilibrium grid spacing for the same case as Fig. 13.

functions of the radial grid density in the stability code for three different equilibria at $\beta_0 = 5.7\%$, each one corresponding to a different sized equilibrium grid. The largest growth rate corresponds to an equilibrium grid of 100 horizontal points, the smallest has 40 points, and the intermediate one has 65 points. Five poloidal mode numbers are included in these calculations, and the unequal spaced radial grid in the stability calculation is concentrated around the singular surface of the strongly dominant mode ($m=3, n=2$). From the figure we conclude that, for this sensitive case, a radial grid with $\Delta\rho \cong 6\times 10^{-4}$ is needed to obtain a converged result. It is also apparent that the equilibrium grid spacing is more important in this case than that employed for the stability calculations.

The converged growth rates (with respect to the stability grid) are plotted versus the equilibrium grid spacing in Fig. 14. The dashed line indicates the extrapolated value of the growth rate to an infinite number of grid points. Thus for a 100×100 grid, which is our standard choice, the error is less than 10%. We emphasize that this result is, however, especially sensitive to the localization of the mode. The same study for the $N=19$ configuration, with a broader eigenfunction does not show any noticeable change in the growth rate value.

The configuration $N=14$ becomes ideally stable at higher beta, entering the second stability regime. The dominant component ($m=3$, $n=2$) of the eigenfunction is plotted versus ρ in Fig. 15 for the previously studied case ($\beta_0 = 5.7\%$) and the case $\beta_0 = 7.9\%$, which is ideally marginally stable. Each point in the figure represents a grid point, and the results are shown in the region of the singular surface for three different grid densities. In the case with $\beta_0 = 5.7\%$, as the grid is refined, a better definition of the peak of the eigenfunction is obtained, and the growth rate converges. Conversely, in the case with $\beta_0 = 7.9\%$, the peak of the eigenfunction is never resolved, and the growth rate decreases strongly as the grid is refined. For clearly unstable modes, such as the $\beta_0 = 5.7\%$ case, the growth rate varies with grid spacing as $\gamma = \gamma_0 + \gamma_2(\Delta\rho)^2$ with $\gamma_0 > 0$ (see, e.g., Fig. 13); while for marginally stable modes the scaling with grid spacing typically is observed to be

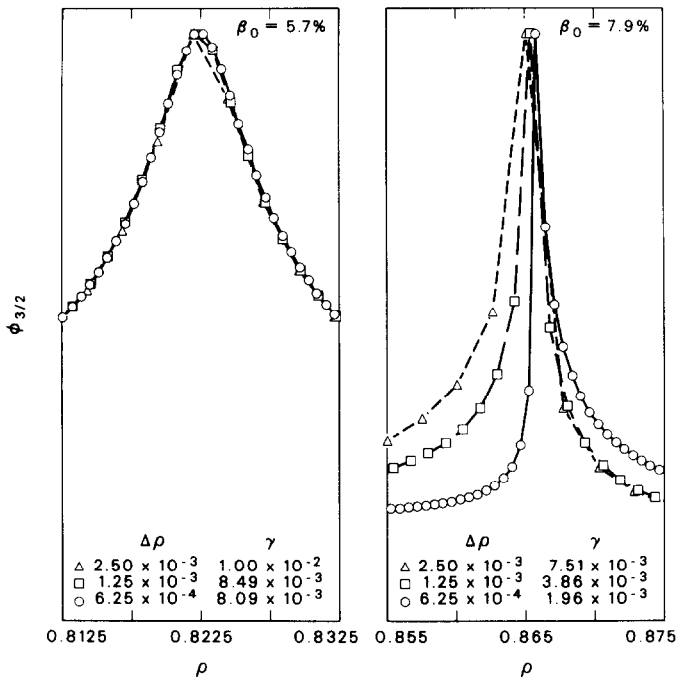

FIG. 15. Grid convergence studies showing the radial behavior of the dominant component ($m = 3$, $n = 2$) for unstable ($\beta_0 = 5.7\%$) and marginally stable ($\beta_0 = 7.9\%$) cases corresponding to the $N = 14$ configuration.

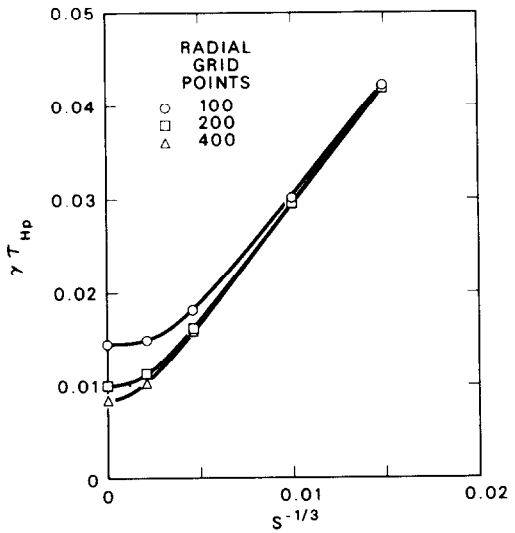

FIG. 16. Linear growth rate of the $n = 2$ mode as a function of S and grid size for the same case as Fig. 13.

$\gamma = \gamma_0 + \gamma_1 \Delta\rho$ with $\gamma_0 \approx 0$. We again emphasize that the sensitivity shown here is observed only for localized modes near the marginal stability limit.

For the case with $\beta_0 = 5.7\%$, we have studied the effect of a small resistivity on the stability behavior. The results are shown in Fig. 16. It is apparent that the introduction of a small resistivity destabilizes the mode. The eigenfunction becomes broader than in the ideal case, and fewer grid points are needed to obtain a converged result. The figure also shows that the numerical diffusion induced by the finite grid is functionally equivalent to a physical resistivity. Unequally spaced radial grids are used in these calculations with 100, 200, and 400 grid points corresponding to $\Delta\rho = 5 \times 10^{-3}$, 2.5×10^{-3}, and 1.25×10^{-3}, respectively, in the region of the singular surface.

To illustrate the convergence studies with respect to the number of modes, we have chosen the configuration $N = 19$, whose eigenfunctions have broad spectra. The results we present correspond to $\beta_0 = 5.6\%$, and 200 equally spaced radial grid points. This number of grid points provides a converged result for this configuration. Figure 17 shows the convergence of the growth rate with respect to the number of modes included in the calculation. It is clear that 10 modes give a converged result.

The spectrum is evaluated using the norm

$$\| \Phi_{mn} \|^2 = \int_0^1 \rho \, d\rho \left[\left(\frac{d\Phi_{mn}}{d\rho} \right)^2 + \frac{m^2}{\rho^2} \Phi_{mn}^2 \right] \tag{59}$$

for each Fourier component. The spectra, normalized to the dominant component, are plotted in Fig. 18 for calculations with differing numbers of modes. It is apparent that the calculation with 10 modes is converged in terms of the spectrum structure.

There is only a factor of four difference between the norms of the largest Fourier component ($m = 2, n = 2$) and the second largest ($m = 3, n = 2$). This suggests that

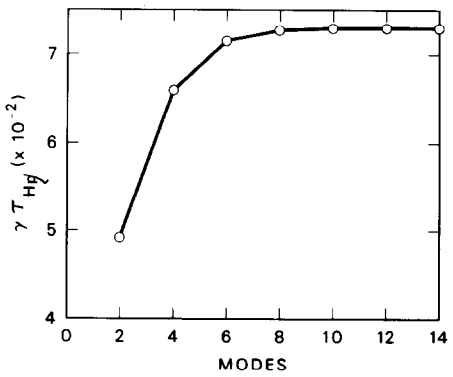

FIG. 17. Linear growth rate of the $n = 2$ mode as a function of the number of poloidal components included in the calculation for the $N = 19$ configuration with $\beta_0 = 5.6\%$.

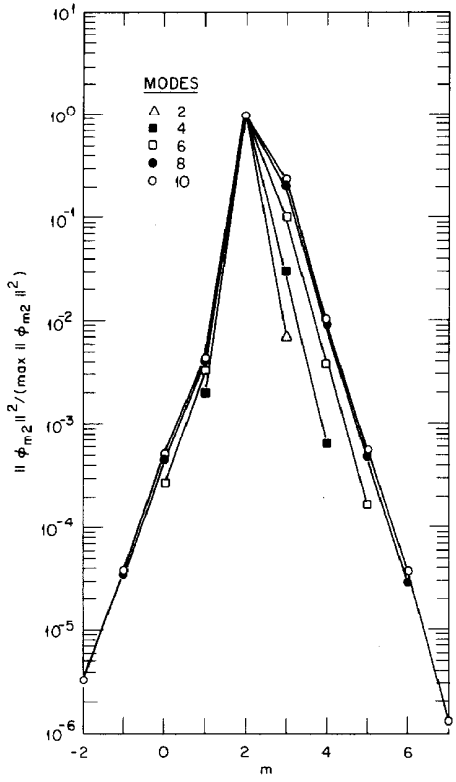

FIG. 18. Poloidal mode number spectra of Φ_{mn} for the same case as Fig. 17.

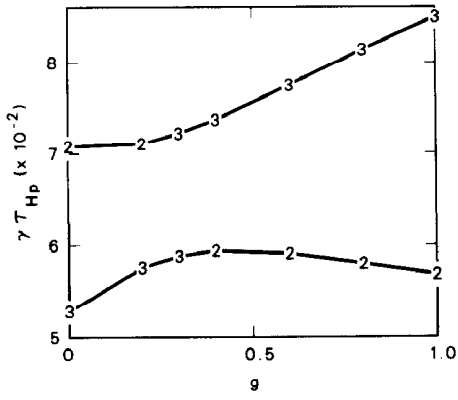

FIG. 19. Linear growth rates of the $n=2$ mode as a function of g for the two most dominant branches. Labels indicate the dominant poloidal component of Φ.

slight changes in the equilibrium profiles can lead to changes in the growth rate and the m-value of the dominant harmonic. To study this, we have parametrically changed the ι profile of the configuration to the profile one would obtain without introducing higher toroidal corrections (i.e., that obtained with constant F). This modification has not been made self consistently in the code because the equilibrium has not been modified, apart from changing the ι-profile. The correction to the ι-profile is of the order of 5%, which leads to a modification in the growth rate of 20%, with the largest harmonic becoming $(m=3,\ n=2)$ instead of $(m=2,\ n=2)$.

Further insight into these sensitivities can be gained by considering the effects of toroidal coupling upon the poloidal components. With the FAR code it is possible not only to determine the fastest growing eigenfunction, but also the more slowly growing subdominant modes [20] having higher radial mode number. The calculation of the second dominant mode, for the above cases involving parametric modification of the ι-profile, gives the largest component of the second dominant mode to be $(m=2,\ n=2)$ for the self-consistent case and $(m=3,\ n=2)$ for the modified case. To determine whether the dominant and second eigenmode branches cross, we have considered several intermediate ι-profiles. The growth rates obtained are plotted in Fig. 19 versus a parameter g that varies from 0 in the case of the original ι-profile to 1 in the case of the modified profile. The intermediate values of g correspond to ι-profiles linearly interpolated between the two extremes. The labels on the curves are the largest poloidal Fourier component of the stream

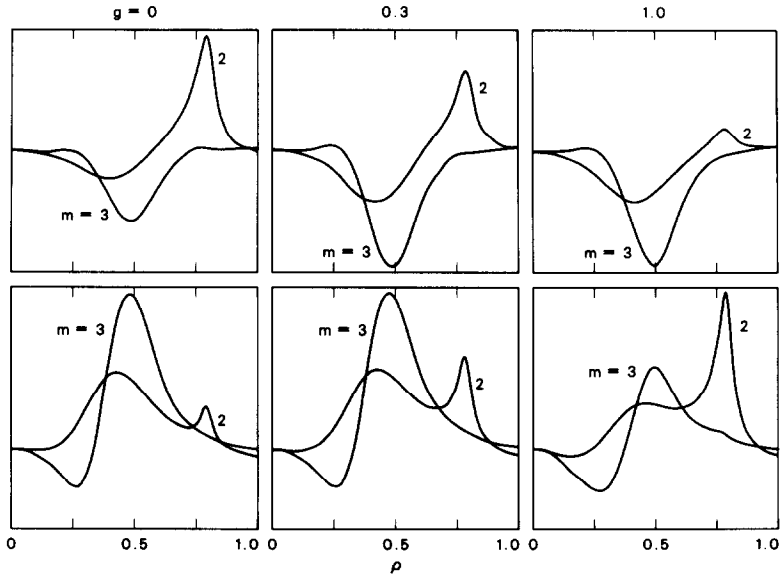

FIG. 20. Poloidal velocity stream function (Φ) as a function of radius for several g values on the first (upper plots) and second (lower plots) branches of Fig. 19.

function Φ, using the norm defined previously. For $g = 0.3$ in both eigenfunctions, the norms corresponding to $m = 3$ and $m = 2$ have practically the same value. What the figure shows is that there is no crossing and, instead, the branches corresponding to the dominant and subdominant modes exchange dominant poloidal components. This is an effect of the coupling of poloidal modes caused by the toroidicity. In the absence of toroidal couplings, each poloidal component would define a set of eigenfunctions decoupled from those of other poloidal components. Numerical calculations, performed without the toroidal coupling terms, show that each poloidal mode number generates a separate eigenmode branch that corresponds, qualitatively, to that obtained by joining together the points in Fig. 19 having the same poloidal mode number. Thus, without toroidal couplings each poloidal mode number defines a branch, and the branches cross as the parametric changes alter the stability of the modes. Introducing the toroidal couplings changes the topology of this picture. The toroidal eigenfunction is a vector composed of different poloidal components, and considering the variation of any single component can be misleading. This is illustrated in Fig. 20 where the eigenfunctions of the $m = 3$ and $m = 2$ components are plotted for three g-values for the dominant and subdominant branches. The ratio between the amplitudes of the $m = 3$ and $m = 2$ poloidal components increases as a function of g in the dominant branch, and decreases in the subdominant branch, but the radial structure of the eigenfunction remains the same in both cases, with the $m = 3$ component having the characteristics of a global mode, while the $m = 2$ component is more localized.

5. SUMMARY

[redacted]

stellarator expansion of Greene and Johnson [5] to calculate equilibrium and stability of configurations having planar magnetic axis variation at moderate and large aspect ratios. In the other approach the assumptions of the stellarator expansion are retained, but the averaging is performed in the magnetic coordinate system of the vacuum fields. This allows the treatment of helical axis systems having toroidally dominated shifts in addition to those configurations amenable to the classical stellarator expansion. Another advantage of the vacuum flux coordinate average method derives from the additional plasma region that is retained by averaging over vacuum flux surfaces, rather than geometric toroidal angle. The drawback of this latter method relates to the additional geometric terms that are required for carrying out the calculations in the generalized coordinate system. Both methods have been implemented using fixed conducting wall boundary conditions.

Both approaches have been implemented to make us of realistic vacuum field information, derived from accurate representations of actual coil configurations. Calculation of the vacuum fields is carried out using the Biot–Savart formula.

Applications have been made to practical design problems as well as to theoretical studies.

Equilibrium calculations using the two average method techniques have been studied [13, 15, 21] both for convergence and for comparison with each other and with other numerical techniques [1–4, 11, 12, 16] (in this work the 3-D NEAR code). For the classical stellarator expansion the numerical β limit of zero net current cases is sensitive to the choice of mesh size, increasing as the mesh is refined. For the magnetic coordinate average method, the observed numerical β limit of $\sim 10\%$ for zero net current cases is related to the appearance of large Pfirsch–Schlüter currents at high β. As in previous work [13, 15, 21], excellent agreement between the results of the different methods was found for applications within their mutual domain of validity.

Stability calculations for low n modes, using the classical stellarator expansion, have been studied for convergence in terms of grid size, poloidal mode truncation, and equilibrium grid. For localized modes, equilibrium and radial grid considerations provide the most stringent convergence considerations, while for global modes the poloidal component representation must be broad ($\gtrsim 10$ modes). The effect of finite grid spacing in stability calculations is to provide a numerical resistivity, which decreases as the grid is refined. For parametric variations in the equilibrium, the growth rates of the dominant and subdominant eigenfunctions (for given n) are found not to cross, although the dominant poloidal components in each eigenmode may be exchanged.

Acknowledgments

This research was sponsored by the Office of Fusion Energy, U.S. Department of Energy, under Contract DE-AC05-84OR21400 with Martin Marietta Energy Systems, Inc.

References

1. F. Bauer, O. Betancourt, and P. A. Garabedian, *A Computational Method in Plasma Physics* (Springer-Verlag, New York, 1978); *Magnetic Equilibrium and Stability of Stellarators* (Springer-Verlag, New York, 1984).
2. R. Chodura and A. Schüter, *J. Comput. Phys.* **41**, 68 (1981).
3. T. C. Hender, B. A. Carreras, L. Garcia, J. A. Rome, and V. E. Lynch, *J. Comput. Phys.* **60**, 76 (1985).
4. S. P. Hirshman and J. C. Whison, *Phys. Fluids* **26**, 3553 (1983).
5. J. M. Greene and J. L. Johnson, *Phys. Fluids* **4**, 875 (1961).
6. N. K. Bogolyubov and Yu. A. Mitropol'skii, *Asymptotic Methods in the Theory of Non-Linear Oscillations* (Nanka, Moscow, 1974).
7. L. M. Kovrizhnykh and S. V. Shchepetov, *Sov. J. Plasma Phys.* **6**, 533 (1980).
8. H. R. Strauss, *Plasma Phys.* **22**, 733 (1980).
9. M. I. Mikhailov, *Sov. J. Plasma Phys.* **6**, 25 (1980).
10. V. D. Pustovitov, *Sov. J. Plasma Phys.* **8**, 265 (1983).

11. G. ANANIA, J. L. JOHNSON, AND K. E. WEIMER, *Phys. Fluids* **26**, 2210 (1983).
12. G. ANANIA AND J. L. JOHNSON, *Phys. Fluids* **26**, 3070 (1983).
13. B. A. CARRERAS, H. R. HICKS, J. A. HOLMES, V. E. LYNCH, L. GARCIA, J. H. HARRIS, T. C. HENDER, AND B. F. MASDEN, *Phys. Fluids* **26**, 3569 (1983).
14. B. A. CARRERAS, H. R. HICKS, J. A. HOLMES, V. E. LYNCH, AND G. H. NEILSON, *Nucl. Fusion* **24**, 1347 (1984).
15. T. C. HENDER AND B. A. CARRERAS, *Phys. Fluids* **27**, 2101 (1984).
16. G. REWOLDT AND J. L. JOHNSON, *Nucl. Fusion* **24**, 733 (1984).
17. R. C. GRIMM, J. M. GREENE, AND J. L. JOHNSON, *Methods in Computational Physics*, edited by J. Killeen (Academic Press, New York, 1976), Vol. 16, p. 253.
18. J. A. HOLMES, Y-K. M. PENG, AND S. J. LYNCH, *J. Comput. Phys.* **36**, 35 (1980).
19. V. E. LYNCH, B. A. CARRERAS, H. R. HICKS, J. A. HOLMES, AND L. GARCIA, *Comput. Phys. Commun.* **24**, 465 (1981).
20. L. A. CHARLTON, J. A. HOLMES, H. R. HICKS, V. E. LYNCH, AND B. A. CARRERAS, *J. Comput. Phys.*, in press.
21. T. C. HENDER, B. A. CARRERAS, L. A. CHARLTON, L. GARCIA, H. R. HICKS, J. A. HOLMES, AND V. E. LYNCH, *Nucl. Fusion* **25**, 1463 (1985).
22. K. UO *et al., in* "Proceedings of the 11th European Conf. on Controlled Fusion and Plasma Physics (Aachen, FRG, September 1983), paper 019.
23. D. K. LEE, *Comput. Phys. Comm.* **25**, 181 (1982).
24. A. E. KONIGES AND J. L. JOHNSON, *Phys. Fluids* **28**, 3217 (1985).
25. A. H. BOOZER, *Phys. Fluids* **25**, 520 (1982).
26. G. KUO-PETRAVIC, A. H. BOOZER, J. A. ROME, AND R. H. FOWLER, *J. Comput. Phys.* **51**, 261 (1983).
27. A. C. HINDMARSH, Lawrence Livermore Laboratory Report, UCID-30150, 1977.
28. D. C. ROBINSON *et al., in* "Plasma Physics and Controlled Nuclear Fusion Research" (IAEA-CN-44/*A*-IV-1, Vienna, 1985), Vol. 1, p. 205.
29. B. A. CARRERAS, H. R. HICKS, AND D. K. LEE, *Phys. Fluids* **24**, 66 (1981).